

Predicting Galaxy Metallicity from Three-Color Images using Convolutional Neural Networks

John Wu^{1*} and Steven Boada¹

¹*Physics and Astronomy Department, Rutgers University, Piscataway, NJ 08854-8019, USA*

Accepted XXX. Received YYY; in original form ZZZ

ABSTRACT

Lorem ipsum dolor sit amet, consectetur adipiscing elit, sed do eiusmod tempor incididunt ut labore et dolore magna aliqua. Ut enim ad minim veniam, quis nostrud exercitation ullamco laboris nisi ut aliquip ex ea commodo consequat. Duis aute irure dolor in reprehenderit in voluptate velit esse cillum dolore eu fugiat nulla pariatur. Excepteur sint occaecat cupidatat non proident, sunt in culpa qui officia deserunt mollit anim id est laborum.

1 INTRODUCTION

Things we are going to want to talk about in the introduction: Morphology-metallicity relation? There is certainly a mass-metallicity relation. Basically, we want to say why we think we can do this at all? What is the primary science driver behind why we think this will work? Is it really just the fundamental plane? We aren't telling the thing about the mass or the distance to the objects.

Spectral super-resolution?

Large-area sky surveys, both on-going and planned, are revolutionizing our understanding of galaxy evolution. The on going Dark Energy Survey (DES; ?) and planned Large Synoptic Survey Telescope (LSST; ?) will survey vast swaths of the sky and create samples of galaxies much larger than any previously know. Spectroscopic follow-up will be key to a deep understanding of the properties of these galaxies, and constrain galaxy evolution (e.g., the mass-metallicity relation, ?; or the fundamental metallicity relation, ??). But as the dataset continues to grow individual follow-up becomes increasingly impractical. Therefore, large spectroscopic surveys are needed to more fully understand the observable-mass relation of clusters. In this work, we propose to use supervised ML, specifically convolution neural networks, to analyze pseudo-three color images to predict galaxy metallicity. This paper is organized as follows: Section ?? we briefly introduce convolutional neural networks, discuss selection of the network's hyperparameters and outline training the network. In Section 3, we describe the acquisition and cleaning of the SDSS data sample. We present the main results in Section 4 and discuss the results in the context of previous works in Section ?. In Section 7, we summarize the key results and conclude. Unless otherwise noted, throughout this paper, we use a concordance cosmological model ($\Omega_\Lambda = 0.7$, $\Omega_m = 0.3$, and $H_0 = 70 \text{ km s}^{-1} \text{ Mpc}^{-1}$), assume a Chabrier initial mass function (?), and use AB magnitudes (?).

2 METHODOLOGY

2.1 Convolutional neural networks

In recent years, neural networks have been able to accomplish a large number of tasks in the field of machine learning (LeCun et al. 1989). Image classification and regression problems are most readily solved by use of convolutions in multiple layers of the network (see, e.g., Krizhevsky et al. 2012). Convolution neural networks (CNNs, or convnets) efficiently learn spatial relations in images whose features are about the same sizes as the convolution filters (or kernels) which are to be learned through training. CNNs are considered *deep* when the number of convolutional layers is large; visualizing their filters reveals that increased depth permits the network to learn more and more abstract features (e.g., from Gabor filters, to geometric shapes, to faces; Zeiler & Fergus 2013).

The input layer is simply an image of 128×128 pixels with three channels (RGB). Dieleman et al. (Galaxy Zoo Kaggle competition) have already shown that CNNs are capable of classifying the morphologies of such images of galaxies from the Sloan Digital Sky Survey (SDSS) with the same accuracy as citizen scientists. Other people have been done other cool things (like use simulated images to select real galaxies, etc). blah blah blah. Define overfitting: a specific and usually not general set of features are learned and misapplied to the test set data.

2.2 Training in practice

We split our training sample of $\sim 130,000$ images into sets of 90,000 for training, 20,000 for validation, and 20,000 for testing. Training images are seen once every epoch, although usually each epoch is split into a number of mini-batches which are learned in parallel. Mini-batches are usually small (256?) and potentially not representative of the full training sample – another technique used to prevent overfitting. Each mini-batch is fed forward through the input layers, where a

random fraction of connections $p = 0.25, 0.50$ are removed between each linear layer (dropout, Hinton et al. 2012; see subsection below). When the feed-forward network reports a prediction, whether a single or set of quantities, then a loss/cost function is used to compute how incorrect the prediction (\hat{y}) is from the true value y . We use the root mean squared error ($\text{RMSE} \equiv \sqrt{\langle |\hat{y} - y|^2 \rangle}$) loss function, and seek to minimize it. We use gradient descent for each mini-batch to adjust each weight parameter, and each fractional contribution of loss is determined by the backpropagation algorithm (cite original, LeCun et al.). The backpropagation algorithm is simply the chain rule applied to finite derivatives, and skipped? for any non-linear layers. The gradient is multiplied by the *learning rate*; batch-normalization is also applied in addition to a momentum term which ensures that the gradient is itself only changing slowly with each mini-batch.

CNNs become difficult to train after many layers are added, likely because the network has already found the best representation possible at a shallower layer, and further layers simply noisily propagate the same signal and degrade the loss. We select an architecture called a residual neural network, or a *resnet* (He et al. 2015), which contains enhanced “shortcut connections” but are otherwise similar to other CNNs. Resnets have been shown to continue learning with increasing depth without the added cost of extra parameters.

We use a 34-layer resnet (He et al.), whose architecture consists of three layer groups. Our resnet is initialized to pre-trained weights from the ImageNet data set, which consists of 1.7 million images belonging to 1000 categories of objects found on Earth (e.g., cats, horses, cars, or books). The earlier layer groups generally have already trained filters that represent low-level abstractions, such as edges or Gabor filters, so we first train only the last layer group of the network (and “freeze” the weights in the first two groups). By reducing the number of trainable parameters, we can rapidly approach the global loss minimum in a few number of epochs. We train the final layers for two epochs using a learning rate of 0.1, and then “unfreeze” the earlier layers and train for another eight epochs using learning rates of [0.001, 0.01, 0.1] for the first, second, and third layer group respectively. For more details about our training methodology, such as the use of learning rate annealing, data augmentation, dropout, batch-normalization, and other hyperparameters, see the Appendix.

Our training methods near convergence after 10 epochs, and additional training only marginally improves the loss. In total, our training steps requires 25-30 minutes on our GPU and uses under 2 GB of memory (depending on batch size). Prediction using data augmentation (see Appendix) takes two minutes for our full test set of 20,466 images, or approximately 6 milliseconds per image (or a little over 1 millisecond per image without augmentation).

In comparison, Huertas-Company et al. 2015 train their network for 10 days on a GPU following the Galaxy Zoo architecture.

We evaluate predictions using not only the RMSE, which approaches the standard deviation for Gaussian-distributed data, but also the NMAD, or the normal median

absolute deviation:

$$\text{NMAD}(x) \approx 1.4826 \times \text{median}(|x - \text{median}(x)|), \quad (1)$$

where for a Gaussian-distributed x , the NMAD will also approximate the standard deviation, σ . NMAD is insensitive to outliers for non-Gaussian distributions and is useful for comparing scatter.

Glossary of terminology:

- Z_{true} is the spectroscopically derived metallicity
- Z_{pred} is the CNN predicted metallicity
- $\Delta Z \equiv Z_{\text{pred}} - Z_{\text{true}}$ is the residual, or error
- $\text{RMSE} \equiv \sqrt{\langle |\hat{y} - y|^2 \rangle}$ is the root-mean squared error. The RMSE loss function is minimized during CNN training.
- $\text{NMAD} \approx 1.4826 \times \text{median}(|x - \text{median}(x)|)$ is the normal median absolute deviation

3 SDSS DATA

Our sample of galaxies are selected from the NYU Value Added Catalog (VAC) [cite](#), to have gas phase metallicities. The 50th percentile metallicity estimates (?) are derived from spectroscopic measurements and for the purposes of this work are assumed to be “the truth.” In addition, we take the derived stellar mass for each galaxy. We supplement the data from the VAC with data from SDSS Data Release 13 (DR13; ?) for each galaxy, the right ascension and declination and the magnitude in each of the five SDSS photometric bands (u, g, r, i, z), along with associated errors. We require that galaxies magnitudes are $10 < u_{\text{griz}} < 25$ mag. Galaxies should have colors $0 < u - r < 6$ [why?](#), high confidence ($z_{\text{err}} < 0.01$) spectroscopic redshifts greater than [0.2](#), [check the petro mags and why we are using those](#).

From this input catalog we create RGB images with the SDSS cutout service¹. Images are scaled to be 128×128 pixels in size, corresponding to $15'' \times 15''$ on the sky. The native $0''.396$ SDSS pixel size are rescaled to $0''.296$ per pixel. We obtain 142,176 three color images to use as the full data set. We split this data set into random 60%, 20%, and 20% subsets, which comprise the training, validation, and test data sets respectively.

4 RESULTS

Examples of the 128×128 pixel *gri* SDSS images seen by the CNN are shown in Figure 1. Rows (a) and (b) depict the galaxies with lowest predicted and lowest true metallicities, respectively. The CNN has associated blue, disk galaxies with low metallicities, and is generally accurate for those which it has identified to be low Z_{pred} . In rows (c) and (d), we show the galaxies with highest predicted and highest true metallicities, respectively. Here we find that red galaxies containing prominent bulges or bright nuclei are predicted to be high in metallicity, and their predictions generally match Z_{true} . The main result appears to be that galaxies predicted by our CNN to have high metallicity ($Z_{\text{pred}} > 9.0$) tend

¹ <http://skyserver.sdss.org/dr14/SkyserverWS/ImgCutout/getjpeg>

to truly have high metallicity, and the equivalent for low-metallicity galaxies. Inversely, galaxies with the *highest* or *lowest* Z_{true} in the sample usually also yield high or low respective predicted metallicities.

We will now consider examples of the most incorrectly predicted galaxies. In rows (e) and (f) respectively, we show instances for which the CNN predicted too low metallicity and too high metallicity. The two galaxies with lowest residuals $\Delta Z \equiv Z_{\text{pred}} - Z_{\text{true}}$ (i.e., most underpredicted metallicities) appear to be suffering from artifacts which cause unphysical color gradients.² Otherwise, the mistakes made by the CNN are similar to ones that human intuition are prone to make: blue, disk sources are generally thought of as lower in metallicity, and redder, more spheroidal objects tend to be higher in metallicity.

In the bottom row (g) of Figure 1, we show five randomly selected galaxies. The random SDSS assortment consists of elliptical, spiral, and possibly even an interacting pair of galaxies. Residuals are low (generally below 0.15 dex), and we again find that the CNN predictions follow human visual intuition.

In the main, larger panel of Figure 3, we compare the distributions of Z_{true} and Z_{pred} using a two-dimensional histogram. We also show the median predictions varying with binned Z_{true} in red, along with the scatter in RMSE (blue) and NMAD (orange), and also the one-to-one line (black). The upper panel shows how the loss varies with spectroscopically derived metallicity. Marker sizes are proportional in area to the number of samples in each Z_{true} bin, and the horizontal lines are located at the average loss (RMSE or NMAD) for the full test data set.

Predictions appear to be both accurate and low in scatter for galaxies with $Z_{\text{true}} \approx 9.0$, which is representative of an average metallicity in the SDSS sample. However, the running median systematically overpredicts metallicity for intrinsically low-metallicity galaxies and underpredicts metallicity for high-metallicity galaxies. We find that the predicted metallicity support is smaller than the range in true metallicity, which flattens the slope of the median Z_{pred} versus Z_{true} relation relative to the one-to-one line. For $Z_{\text{pred}} > 9.1$ or $Z_{\text{pred}} < 8.5$, CNN predictions are difficult to trust, although this only comprises 20% of our test data set.

although the CNN generally predicts from a more limited range of metallicity (i.e., $8.1 < Z_{\text{pred}} < 9.2$) than is evident from the true metallicity range (where $Z_{\text{true}} < 8.0$ or $Z_{\text{true}} > 9.4$ is possible). See Figure 2 for more...

Note that the global NMAD (0.0668) is higher than the weighted average of the binned NMAD (~ 0.05). This is due to the fact that e.g., a residual $\Delta Z \approx 0.2$ would be treated as an outlier at $Z_{\text{true}} = 9.0$, where the CNN is generally accurate, but the same residual would not be rejected as an outlier using NMAD for $Z_{\text{true}} = 8.5$. Since the binned

average NMAD depends on choice of bin size, we do not include those results in our analysis.

4.1 Diagnostics

We consider the effects of image resolution by running the exact same CNN training and test procedure on the same images scaled to different sizes. Our initial results use SDSS $15'' \times 15''$ cutouts resized to 128×128 pixels, and we now downsample the images to 64×64 , 32×32 , \dots , 2×2 , and even 1×1 pixels. All images retain their three channels, so the smallest 1×1 image effectively contains three colors of the image (averaged together with its background and possible neighboring sources).

In Figure 4, we compare predictions with truths at each resolution by measuring the scatter in ΔZ using the RMSE and NMAD metrics. The global scatter is reported here, such that outliers are identified from the residual distributions over the full test set. Also shown is the resulting scatter in ΔZ if we had always predicted the mean value of Z_{true} over the data set (which is very close to the mean value of the training data set), which provides a baseline comparison to a zeroth-order prediction. We find that both RMSE and NMAD decrease with increasing resolution. The scatter is a strong function of resolution as the images are resolved from 2×2 to about 32×32 . With further increasing resolution, improvement is still evident, although the scaling with scatter is weaker than at lower resolution.

There appears to be a huge improvement between the baseline $Z_{\text{pred}} = \langle Z_{\text{true}} \rangle$ prediction and the 1×1 CNN prediction, but seemingly little improvement going from 1×1 to 2×2 pixel images. This finding should not surprise us, however. 1×1 three-color images contain similar information to three photometric data points (although because of the averaged background and neighboring pixels, it is less useful than photometry), and three photometric data points can be used to perform a crude spectral energy distribution (SED) fit. The color information is useful enough to create an approximate color-magnitude diagram, and each galaxy's position in this parameter space correlates with Z_{true} . The 2×2 three-color images contain four times as many pixels as the 1×1 images. However, because there is an even number of pixels, this information is still averaged between all available pixels, as so the incremental gain is small!³

For all CNN predictions, the NMAD is lower than the RMSE by a factor of 0.75 – 0.80. **How can we interpret this?**

4.2 Comparisons to Previous Works

Lorem ipsum dolor sit amet, consectetur adipiscing elit, sed do eiusmod tempor incididunt ut labore et dolore magna aliqua. Ut enim ad minim veniam, quis nostrud exercitation ullamco laboris nisi ut aliquip ex ea commodo consequat. Duis aute irure dolor in reprehenderit in voluptate velit esse

² Note that both are labeled as quasars according to their SDSS DR14 spectra. **A. Baker mentioned that it is possible some of the incorrect predictions in Figure 1 may be due to the fact that the R_{23} estimator is a double-valued function, and the particular branch chosen may cause incorrect estimation of Z_{true} . Such an effect may be possible if, e.g., one of the oxygen lines is at low SNR and the uncertainties are large.**

³ There is extra information in the 2×2 pixel images in non-circularly symmetric cases. For an inclined disk, it is possible to roughly determine the orientation in the sky plane, but this information is not very useful. In the case of a major merger or interacting companion, the 2×2 images may be more powerful than 1×1 images.

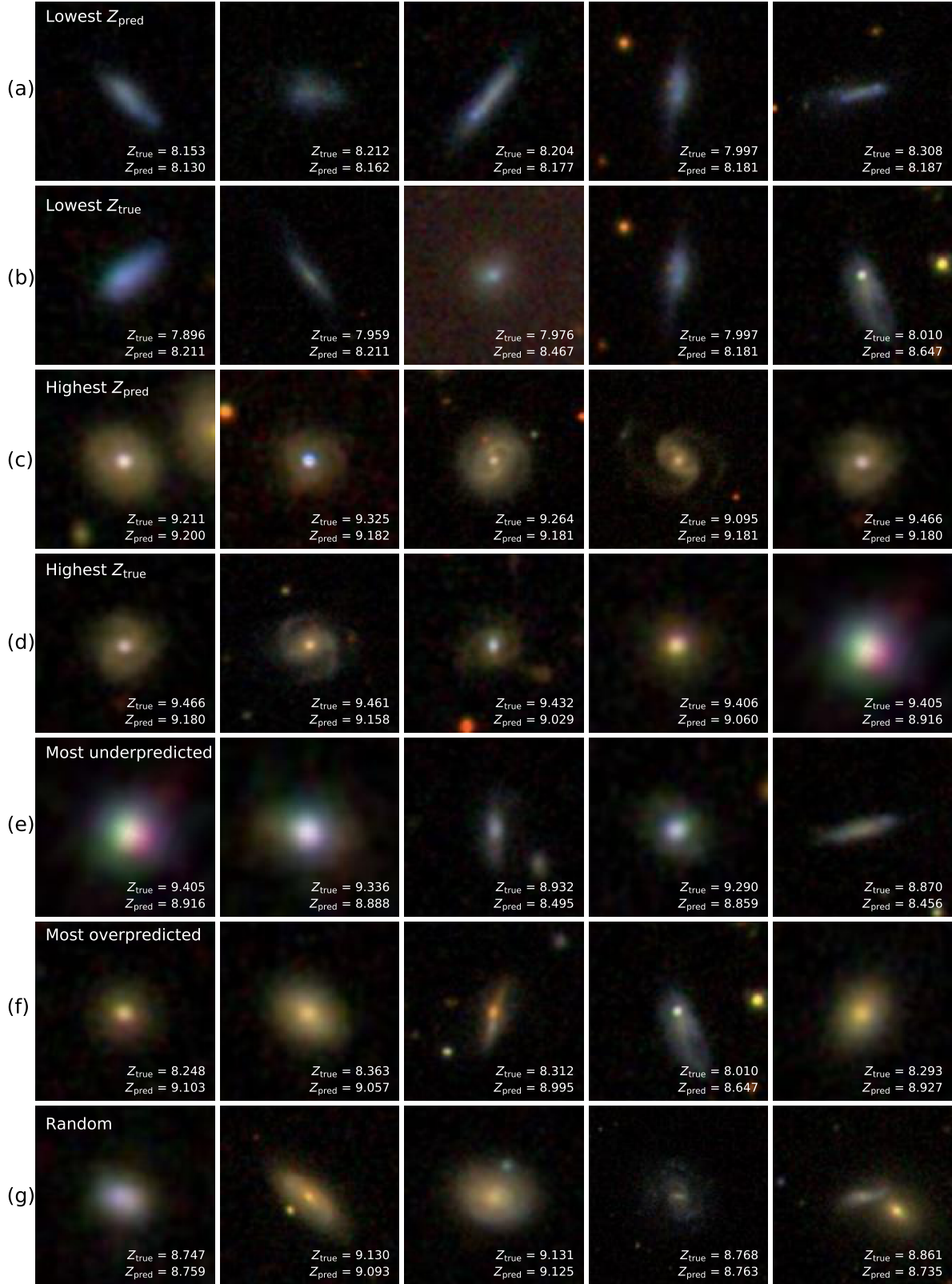


Figure 1. SDSS imaging with predicted and true metallicities from the test data set. Five examples are shown from each of the following categories: (a) lowest predicted metallicity, (b) lowest true metallicity, (c) highest predicted metallicity, (d) highest true metallicity, (e) most negative $\Delta Z \equiv Z_{\text{pred}} - Z_{\text{true}}$, (f) most positive ΔZ , and (g) randomly selected galaxies.

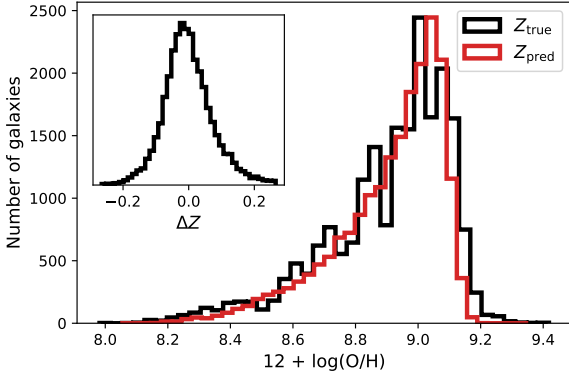


Figure 2. The metallicity distributions.

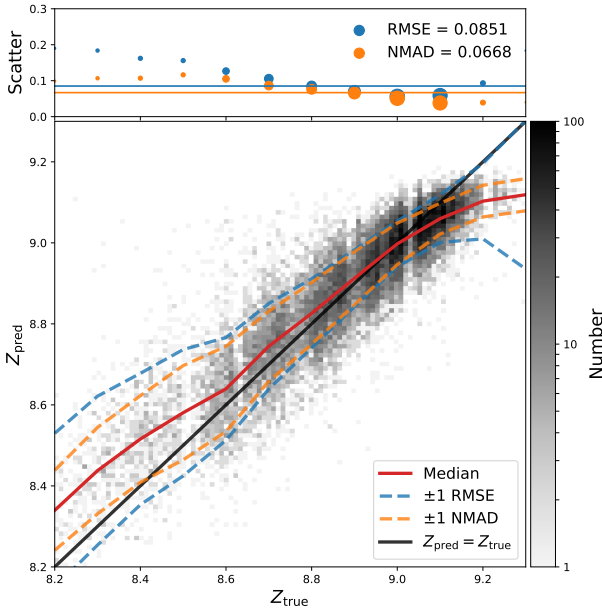


Figure 3. Bivariate distribution of metallicity truths (Z_{true}) and CNN predictions (Z_{pred}) are shown in the main panel. Overlaid are the predicted median metallicity (solid red line), RMSE scatter (dashed blue line), NMAD scatter (dashed orange line) in bins of Z_{true} , and a one-to-one relation (solid black line). In the upper panel, we again show the binned scatter, where the size of each marker is proportional to the number of galaxies in that bin. Each horizontal line corresponds to the average scatter over the entire test data set (and global value indicated in the upper panel legend).

cillum dolore eu fugiat nulla pariatur. Excepteur sint occaecat cupidatat non proident, sunt in culpa qui officia deserunt mollit anim id est laborum.

Obviously compare with Huertas-Company et al. Also look at Viviana’s work as benchmark. Compare with Galaxy Zoo as well. Maybe CMU Deeplens paper for finding Einstein rings/arcs. Note work from Sara Ellison’s group: 2016MNRAS.455..370E, 2017MNRAS.464.3796T, 2016MNRAS.457.2086T

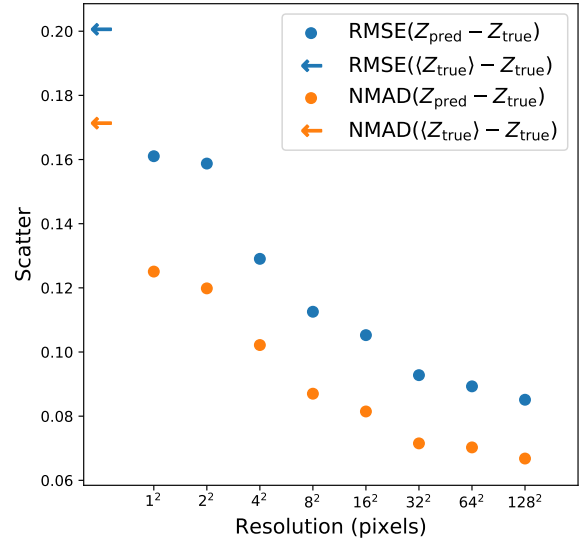


Figure 4. The effects of image resolution on CNN performance. Blue and orange circular markers indicate scatter in the residual distribution (ΔZ) measured using RMSE and NMAD, respectively. (Each point is analogous to the horizontal lines shown in Figure 3.) We also show arrows marking the “baseline” values for only predicting the mean of the Z_{true} distribution, i.e., if no information about the image is known.

5 THE MASS-METALLICITY RELATION

- $M_{*, \text{true}}$
- $M_{*, \text{pred}}$
- MZR, the mass-metallicity relation from Tremonti et al. (2004)
- $Z_{\text{MZR}} =$

Given the low scatter in metallicity residuals (predicted – true), we consider if the CNN is able to accurately predict stellar mass, and then leverage the mass-metallicity relation (MMR; Tremonti et al. 2004) to infer metallicity. Alternatively, if SFR and M_* are learned, then the fundamental metallicity relation (FMR; Mannucci et al. 2010, Lara-Lopez et al. 2010) may explain low residuals.

If there existed a fourth parameter, perhaps morphological in nature, then the marginalized MMR or FMR over particular values of this fourth parameter should be an even tighter relationship. Such a result would be analogous to how the MMR at any given star formation rate (SFR) has smaller scatter than over all SFRs.

We find that the MMR constructed using SDSS-measured metallicity (via R_{23}) and the MMR constructed using CNN-predicted metallicity (from gri imaging) are quantitatively different. In both cases we have used the GalSpecExtra catalog for stellar masses. The MMR using CNN metallicity has smaller scatter, where the weighted average ratio of scatter is $\text{NMAD}(\text{CNN})/\text{NMAD}(\text{SDSS}) = 0.821 \pm 0.077$.

We also produced plots of the MMR using SDSS- and CNN-predicted masses, and SDSS metallicity from the Gal-

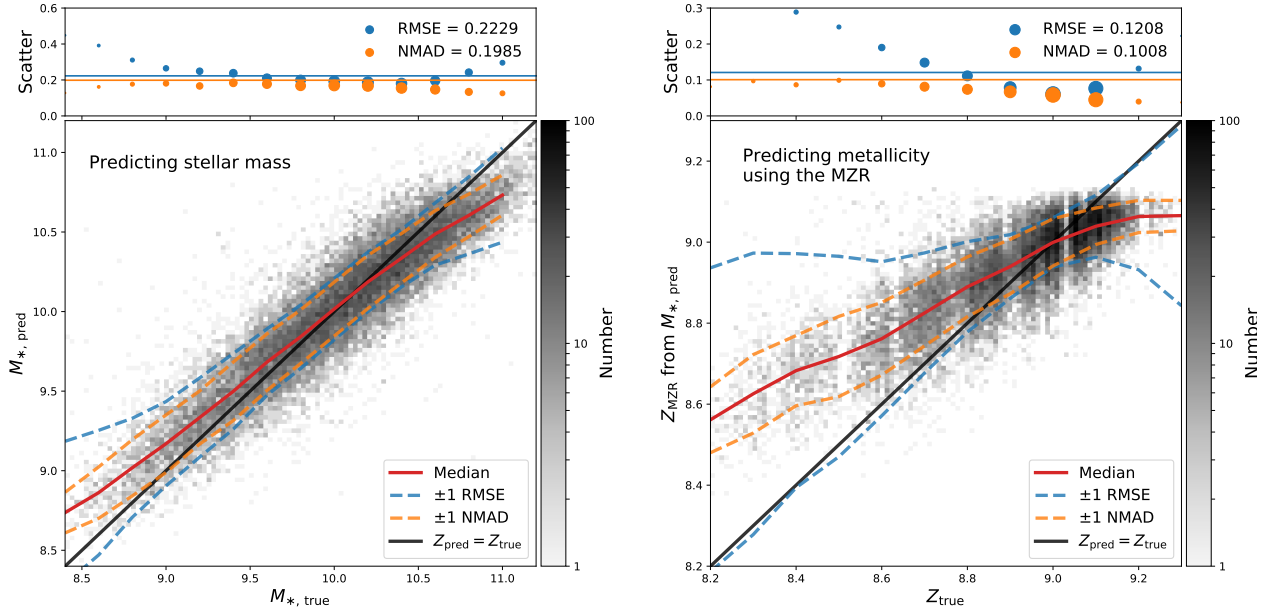


Figure 5. In the left subplot, we show predicted against true stellar mass. Colors and marker or line styles are the same as in Figure 3. If the right subplot, we compare the predicted stellar mass converted to metallicity, assuming the Tremonti et al. mass-metallicity relation (MZR), with the true metallicity.

SpecExtra catalog. Here the scatter in metallicity at given mass is again lower when using CNN predictions than for SDSS measurements. The scatter is smaller by a factor $\text{NMAD}(\text{CNN})/\text{NMAD}(\text{SDSS}) = 0.811 \pm 0.057$.

It is possible that the metallicity depends on some morphological component in addition to the emission lines informing the spectroscopic measurement. However, we believe that the qualitatively accurate MMR is actually artifact of the CNN’s limitations rather than its strengths. Instead of finding a more fundamental representation of metallicity, the CNN likely detects the stellar mass. In the case of using our CNN to predict metallicity, the slope of the MMR is shallower than from the “true” data. However, when the CNN is used to predict mass, the slope of is too steep. This effect is driven by the fact that the CNN is unable to predict the full range of metallicities or masses, since the fraction of training examples at extremely low or high values is small. **Therefore, the scatter in all of its predictions is narrower, such that when it predicts metallicity, the truncated range forces the MMR relationship to appear shallower, and when the CNN predicts M_* , the limited range in mass cause the MMR relationship to appear steeper.**

Why then does the MMR hold at all? For if the CNN predicts, e.g., too narrow a distribution of metallicity, then what prevents those predictions from scattering over the full range in stellar mass? The answer is quite possibly that the CNN only “sees” the metallicity via the stellar mass, such that the predicted MMR is effectively a relationship between the predicted mass and the true mass. This theory is bolstered marginally by the fact that the fraction scatter for predicting mass is lower than for predicting metallicity (albeit not significantly so). More intuitively, we might believe that the CNN can “see” that read and dead elliptical galaxies are higher in stellar mass, and that blue irregulars are lower

in stellar mass. Then the CNN simply needs to propagate the mass prediction through the tight ~ 0.1 dex MMR.

How then can we achieve a $\text{NMAD} = 0.067$ dex in metallicity by noisily propagating a signal with $\text{NMAD} = 0.22$ scatter through the MMR which has 0.1 dex intrinsic scatter (Tremonti et al. 2004)?

M/L ratio of redder galaxies are higher at fixed luminosity (Bell & de Jong 2001; Kauffman+03).

6 FUTURE APPLICATIONS

Lorem ipsum dolor sit amet, consectetur adipisicing elit, sed do eiusmod tempor incididunt ut labore et dolore magna aliqua. Ut enim ad minim veniam, quis nostrud exercitation ullamco laboris nisi ut aliquip ex ea commodo consequat. Duis aute irure dolor in reprehenderit in voluptate velit esse cillum dolore eu fugiat nulla pariatur. Excepteur sint occaecat cupidatat non proident, sunt in culpa qui officia deserunt mollit anim id est laborum.

7 SUMMARY

Lorem ipsum dolor sit amet, consectetur adipisicing elit, sed do eiusmod tempor incididunt ut labore et dolore magna aliqua. Ut enim ad minim veniam, quis nostrud exercitation ullamco laboris nisi ut aliquip ex ea commodo consequat. Duis aute irure dolor in reprehenderit in voluptate velit esse cillum dolore eu fugiat nulla pariatur. Excepteur sint occaecat cupidatat non proident, sunt in culpa qui officia deserunt mollit anim id est laborum.

Our main conclusions are the following:

- (i) Lorem ipsum dolor sit amet, consectetur adipisicing elit, sed do eiusmod tempor incididunt ut labore et dolore

magna aliqua. Ut enim ad minim veniam, quis nostrud exercitation ullamco laboris nisi ut aliquip ex ea commodo consequat. Duis aute irure dolor in reprehenderit in voluptate velit esse cillum dolore eu fugiat nulla pariatur. Excepteur sint occaecat cupidatat non proident, sunt in culpa qui officia deserunt mollit anim id est laborum.

(ii) Lorem ipsum dolor sit amet, consectetur adipisicing elit, sed do eiusmod tempor incididunt ut labore et dolore magna aliqua. Ut enim ad minim veniam, quis nostrud exercitation ullamco laboris nisi ut aliquip ex ea commodo consequat. Duis aute irure dolor in reprehenderit in voluptate velit esse cillum dolore eu fugiat nulla pariatur. Excepteur sint occaecat cupidatat non proident, sunt in culpa qui officia deserunt mollit anim id est laborum.

ACKNOWLEDGEMENTS

The authors also wish to thank the anonymous referee whose comments and suggestions significantly improved both the quality and clarity of this work. The authors also thank David Shih and Matthew Buckley for use of their GPU cluster at Rutgers University High Energy Experimental Physics department. This research made use of the IPYTHON package (?) and MATPLOTLIB, a Python library for publication quality graphics (?). Funding for the SDSS and SDSS-II has been provided by the Alfred P. Sloan Foundation, the Participating Institutions, the National Science Foundation, the U.S. Department of Energy, the National Aeronautics and Space Administration, the Japanese Monbukagakusho, the Max Planck Society, and the Higher Education Funding Council for England. The SDSS Web Site is <http://www.sdss.org/>.

APPENDIX A: RESIDUAL CONVOLUTIONAL NEURAL NETWORKS

We find that a 34-layer resnet (Resnet-34) architecture can be trained efficiently on a Pascal P100 with 16 GB of memory. Using the hyperparameters described below, an epoch takes about 60 seconds to train. We initialize our resnet with pretrained weights from the ImageNet (Russakovsky et al. 2014; He et al. 2015) 1.7 million image data set trained to recognize 1000 classes of objects found on Earth (i.e., cats, dogs, or cars). In practice, the filters learned through the early layers of the pretrained CNN can be used for other image recognition tasks, aptly named “transfer learning” (cite).

A1 Hyperparameter selection

A2 Data augmentation

Nearly all neural networks benefit from larger training samples because they help prevent overfitting. Outside of the local Universe, galaxies are seen at nearly random orientation; such invariance permits synthetic data to be generated from rotations and flips of the training images. Each image is fed into the network along with four augmented versions, thus increasing the total training sample by a factor of five. This technique is called data augmentation, and is particularly helpful for the network to learn uncommon or unrepresented truth values (e.g., in our case, very metal-poor

or metal-rich galaxies). Each training-augmentation is fed forward through the network and gradient contributions are computed together as part of the same mini-batch. A similar process is applied to the network during predictions, which is called test-time augmentation (TTA). Synthetic images are generated according to the same rules applied to the training data set. The CNN predicts an ensemble average over the augmented images. It has been found that data augmentation improves predictions by as much as $\sim 20\%$ (cite).

A3 Cyclical learning rate annealing

The learning rate determines how large of a step each network weight takes in the direction of the backpropagated error. A large learning rate thus forces the weights to make large updates, which generally prevents overfitting but also may cause the parameters to overshoot minima in the loss function landscape. A small learning rate may allow the weights to get stuck in a local minima near their initial positions, or also might cause the network to learn very slowly. The number of local minima increases exponentially with dimensionality (cite), so selecting a low learning rate does not ensure that the network will eventually make it to near the global minimum. Therefore, it is often useful to anneal, or reduce, the learning rate from a high value in the beginning – which allows the weights to find the right ballpark values – to a low value – which allows the weights to take finer steps near the global minimum – over the course of multiple training epochs.

In practice, annealing can be enforced manually, e.g., the learning rate might be reduced by a factor of 10 every time the loss function plateaus over a number of epochs. Eventually even reduced learning rates do not permit additional improvement of the loss, and so the training period is concluded. We instead use a method called cosine annealing, during which the learning rate is annealed continuously over one or more epochs for *each* mini-batch until it eventually reaches zero.

We employ stochastic gradient descent with restarts (SGDR), over progressively longer training cycles, and restart cosine annealing over each cycle (Leslie Smith 2015?). For example, the first cycle comprises one epoch during which the learning rate is cosine annealed. It then trains for another cycle with cosine annealing, which starts at the same learning rate but is annealed over twice the duration (two epochs). These “restarts” have been shown to kick the weights configuration out of saddle points in the loss of some high-dimensional parameter space. Training can then proceed past what appear to be local minima but are actually saddle points (where gradient descent generally performs poorly).

A4 Layer learning rates

ADD MORE HERE

Frozen training to get final activates in right “ballpark.” We then unfreeze all layers and train using different rates in different layer groups.

A5 Batch normalization and Dropout

Batch normalization (BN; 1502.03167) is a technique developed to fix the vanishing gradients problem which make deep networks inefficiently slow to train. The issue arises when gradients are backpropagated through deep neural networks to update weights, and loss contributions become vanishingly small except only when the weights have small magnitudes. Normalizing the inputs to each mini-batch mean and standard deviation somewhat remedies the problem, and has been applied to (convolutional) neural networks since the 1990s. BN extends this normalization to all activations in hidden layers, thus adding two hyperparameters which modulate the mean and standard deviation of each layer to zero and unity, respectively. The BN hyperparameters are learned for each mini-batch and are updated in addition to weight parameters during the backward pass.

Without BN, activations in any given layer may span a large range and contributions from certain parts of the network may become dwarfed by others. After the normalization step, all pre-activations are on the same scale and thus gradient descent steps can more efficiently traverse the loss function space. Training proceeds more rapidly and converges toward a solution more quickly. Choice of mini-batch size also impacts the learning rate, as small batch size increases stochasticity in each gradient. Large batch size allows for better parallelization on the GPU and ensures smoother gradients. We note that smooth gradients across mini-batches can prevent the solution from hopping out of local basins, and negatively impact performance. Increasing the learning rate as batch size is increased can resolve this problem, at least in part, but limits the convergence ability of the network (until the rate is annealed). We find in practice that batch sizes between 128 and 512 work best at balancing noisy gradients and learning rate.

Dropout is a method of disabling a random subset of connections after linear layers for each mini-batch (Hinton et al. 2012). By removing random connections between fully-connected layers, dropout effectively treats each mini-batch as one in an ensemble of random training subsets. It is instructive to think of each mini-batch in the full training data as analogous to a decision tree in a random forest. The ensemble of learned gradients is less prone to overfit the training data set because the network is forced to discard random (and potentially valuable) information. The resulting network is better able to, for example, learn subtle differences in the data that would otherwise be ignored when more obvious features dominate the gradient descent process. Since our Resnet architecture is broadly separated into multiple groups of layers, we can apply lower dropout rate at earlier layers in order to ensure that those filters are learned more quickly. Using a differential dropout rate is sensible because filters learned in the first few layers of the network tend to be Gabor filters and edges in general, and there is little risk of overfitting when such low-level abstractions are always necessary for learning high-level features in the middle and final layers.

During validation and testing, dropout is not used because all of the data is useful for predictive power. We use dropout rates of 0.25 for the linear layer after the early group, and 0.50 at the later linear layer. We find that dropout combined with BN – although not recommended

in the original paper – work in tandem to boost training speeds and avoid overfitting.

This paper has been typeset from a $\text{\TeX}/\text{\LaTeX}$ file prepared by the author.